Steel and Composite Structures, *Vol. 34, No. 6* (*2020*) *877-889*
DOI: https://doi.org/10.12989/scs.2020.34.6.877

Investigating loading rate and fibre densities influence on SRG - concrete bond behaviour

Hashem Jahangir[a] and Mohammad Reza Esfahani*

Department of Civil Engineering, Ferdowsi University of Mashhad, Azadi Square, Mashhad, Razavi Khorasan, Iran

(*Received July 29, 2019, Revised October 16, 2019, Accepted October 21, 2019*)

Abstract. This work features the outcomes of an empirical investigation into the characteristics of steel reinforced grout (SRG) composite - concrete interfaces. The parameters varied were loading rate, densities of steel fibres and types of load displacement responses or measurements (slip and machine grips). The following observations and results were derived from standard single-lap shear tests. Interfacial debonding of SRG - concrete joints is a function of both fracture of matrix along the bond interface and slippage of fibre. A change in the loading rate results in a variation in peak load (P_{max}) and the correlative stress (σ_{max}), slip and machine grips readings at measured peak load. Further analysis of load responses revealed that the behaviour of load responses is shaped by loading rate, fibre density as well as load response measurement variable. Notably, the out-of-plane displacement at peak load increased with increments in load rates and were independent of specimen fibre densities.

Keywords: bond properties; failure mode; steel reinforced grout (SRG); single-lap shear test; concrete substrate

1. Introduction

Given the favourable strength-to-weight ratio, engineerable mechanical properties and comparatively fast cure time, fibre-reinforced composites have been a prime reinforced concrete (RC) strengthening material. Fibre-reinforced polymer (FRP) is presently the most prevalent structural composite technology. FRP composites constitute of organic thermoset resin as the matrix/binders and continuous fibres (commonly basalt, glass, carbon or aramid fibres) (Bagheri *et al.* 2019). If the presence of organic binders in FRP is a constraint (ACI 440.2R 2008), fibre-reinforced cementitious matrix (FRCM) composites, which is made up of continuous fibers (for instance, polyparaphenylene benzo-bisoxazole (PBO)) and inorganic cementitious binding agents instead, could be an alternative.

Correspondingly, the incorporation of high-strength steel fibres as a complementary material to FRP systems is increasingly viable as an economical substitute to the conventional fibres described earlier. Notably, the applications of steel-reinforced polymer (SRP) and steel-reinforced grout (SRG) have been published since 2002 (Pellegrino and Modena 2002, Huang *et al.* 2005, Lopez *et al.* 2007). In this paper, the former describes a composite with steel fibres or fabrics embedded in a polymer matrix. As for the latter, the term is used when an inorganic matrix is used as a substitute for epoxy in a composite. Research on SRP and SPG has focused mainly on their mechanical properties (Razavizadeh *et al.* 2014, De Santis *et al.* 2016, Cao *et al.* 2017, Kwon *et al.* 2018, Mazzuca *et al.* 2019) as well as bond behaviour on concrete (Huang and Huang 2011, Jabbar *et al.* 2016, Ascione *et al.* 2017, Koutas *et al.* 2019, Ascione *et al.* 2019), clay brick and masonry substrates (Grande *et al.* 2015, De Santis *et al.* 2017, De Santis *et al.* 2018, Casadei and Girardello 2019). In addition, large scale experiments have demonstrated the effectiveness of both technologies in strengthening RC beams (Park *et al.* 2007, Bencardino and Condello 2014, Aggelis *et al.* 2016, Jiang *et al.* 2017, Sumathi and Vignesh 2017, Liang and Xing 2018, Barakat *et al.* 2019), masonry arches (Borri *et al.* 2009, Alecci *et al.* 2016, Carozzi *et al*. 2018;, De Santis *et al*. 2019) and walls (Li *et al.* 2012, Koksal *et al.* 2013, De Canio *et al.* 2016, Babatunde 2017, Wang *et al.* 2018, Mazzuca *et al.* 2019). It is, however, cautioned that debonding failure will inherently affect the superior strengthening performance of SRP and SRG systems. A unique exception is observed in composites with relatively low fibre density (Jabr *et al.* 2017). While SRP debonding often arises within a fine matrix-rich layer of RC, SRG debonding could develop within the composite itself. Despite the wide-ranging field applications of composites (Park and Yoo 2015, Hadji *et al.* 2016, Prashob *et al.* 2017, Abderezak *et al.* 2018, Casadei and Girardello 2019), there are several compelling knowledge gaps which remained to be addressed.

The fibre density and the loading rate are two important considerations in the study of the behaviour of FRCM-to-concrete interfacial bonds. Amidi and Wang (2016) and Salimian and Mostofinejad (2019) revealed that bond capacity, the maximum interfacial shear stress, and interfacial fracture energy are highly influenced by the strain rate. The effects of strain rate on both FRP-to-concrete bonds and bare concrete are analogous (Salimian and Mostofinejad 2019). In the physical assessment of

*Corresponding author, Professor
E-mail: esfahani@um.ac.ir
[a]Ph.D.

ISSN: 1229-9367 (Print), 1598-6233 (Online)

strain rates through direct-shear tests, a constant displacement rate does not entail a constant strain rate. Strain rate effects are particularly evident in joints of inferior structural strength (Amidi and Wang 2016) and are independent of the kind of polymeric binders utilized.

In order to do a multi-parametric research work on bond behavior of steel reinforced grout composites, in this paper, direct shear tests were conducted on concrete blocks strengthened by externally bonded SRG composites strips to investigate the effects of rate on the control parameter. Three distinctive fibre densities, corresponding to low density (LD), medium density (MD) and medium-high density (MHD), and two categories of measurement (slip and machine grips) were evaluated in this work. Slip was derived by methodically raising the mean of two linear variable displacement transducers (LVDT) readings taken at the start of the SRG bonded region. Machine grips denoted the displacement response obtained by an LVDT insert in the machine head. Regardless of the fibre densities, bond width was fixed to be 50 mm whereas two bond lengths (200 mm and 450 mm) were used.

2. Materials and methods

2.1 Material properties

Concrete specimens, which were either used directly for the shear tests or as samples for characterization of material properties, were casted from eight different batches of nominal density concrete and Portland cement. The concrete batches was mixed using constituent proportions of cement (1.00), water (0.55), coarse aggregate (2.50) and fine aggregate (3.00). The coarse aggregate comprised of river gravel with a maximum size of 15 mm. The average compressive (EN 12390-3 2009) strength of the concrete samples at 28 days, derived from a series of twenty-four compressive tests (three for each batch) and administered on 150 mm × 150 mm × 150 mm cubes , measured at 23.69 MPa (CoV = 0.073).

The SRG composite constituted of a single layer of ultra-high strength galvanized steel fibres combined with an inorganic mortar matrix. The fibre layer was made up of unidirectional sheets of steel micro-cords attached to a fibreglass micromesh. Each fibre was an assemble of three straight filaments and two wrapped filaments with a working cross sectional cord area (A_{cord}) of 0.538 mm^2.

Table 1 Mechanical properties and technical specifications of steel fibres (Kerakoll 2018)

Property	Low density	Medium density	Medium-high density
Number of cords/mm	0.157	0.235	0.314
Tensile strength (MPa)	>3000	>3000	>3000
Modulus of elasticity (GPa)	>190	>190	>190
Ultimate strain (%)	>2	>2	>2
Equivalent thickness (mm)	0.084	0.126	0.169

Table 2 Mechanical properties of mortar matrix (Kerakoll 2018)

Property	Mortar matrix
Compressive strength at 28 days (MPa)	>50
Tensile strength at 28 days (MPa)	>10
Flexural strength at 28 days (MPa)	>9

Based on the manufacturer’s report (Kerakoll S.p.A., 2018), the LD, MD and MHD fibre sheets measured at 0.157 cords/mm, 0.235 cords/mm and 0.314 cords/mm, respectively. The technical specifications and mechanical properties of the steel fibres and mortar mix in this work are reported in Tables 1 and 2, accordingly.

2.2 Test set-up

The single-lap shear test was conducted to investigate the debonding mechanism between the SRG and RC substrates. Twenty-one concrete prisms measuring 150 mm in width, 600 mm in length and 150 mm in depth were used as specimens. Within 300 to 350 days post-casting, the prisms were first sandblasted with silica sand prior to being reinforced with SRG strips through a wet-lay process (Kerakoll 2018). The laboratory curing period for all SRG-concrete specimens was up to 28 days post-casting at standard environmental condition (ambient temperature of 20℃ with 60% humidity).

SRG strips were applied onto a single face on each specimen. An inorganic mortar was coated on a dedicated bonding area to embed the fibres and secure the strip. Any excess fibres beyond that region was left exposed. The width-wise fibre configuration of the reinforcement was intentionally set to provide a half-of-the-fibre-spacing allowance between the outer fibres and the boundaries of the matrix. The inorganic mortar layers were 4 mm thick, which implied that the composite strip had total thickness of about 8 mm. The bonding area commenced at a 35 mm mark from the top corner of the loaded end of the fibres to provide an interfacial indentation. Following the conventional push-pull arrangement, the concrete prisms were restrained from moving while the fibres were pulled in one direction. For pulling, a thermosetting epoxy tab measuring 75 mm in length was placed at the edge of the fibre strips to remove the need of additional auxiliary handlers.

The concrete prisms were fixed in position with a pair of steel plates placed on its top and bottom flat surfaces. The underside plate was fastened to a cylindrical steel member held in place by the bottom wedges of the testing machine. As for the topside plate, a C-shaped steel element was designed to have its centroid as close as possible to the centroid of the underside plate, to reduce any undesired effects of the eccentricity during the shear tests. The top and bottom plates were connected to each other with four steel bars as shown in Fig. 1.

Each steel bar was fixed with three strain gauges that were aligned to its longitudinal axis and arranged 120° apart. The resulting strain responses were averaged to

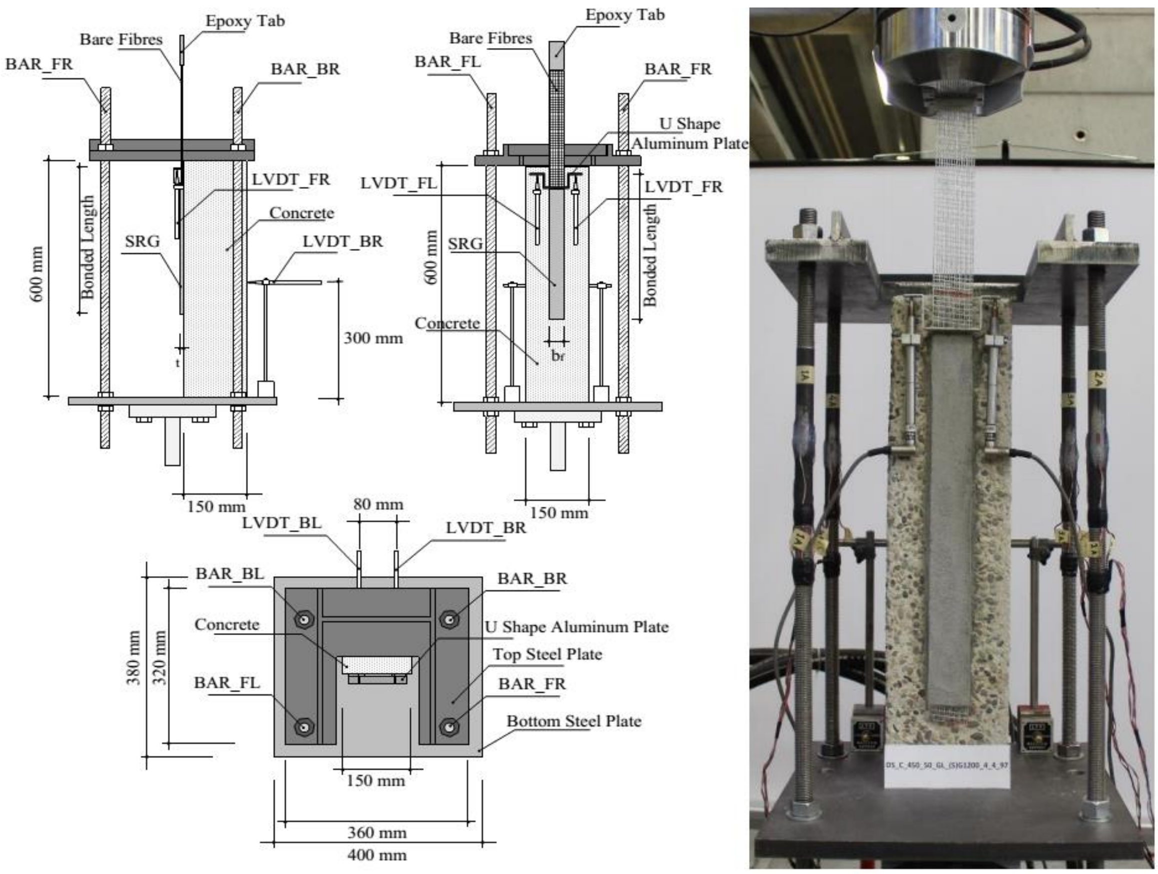

(a) (b)

Fig. 1 (a) Test set-up and (b) Picture of the SRG specimen S_MHD_R10_1

obtain a representative strain estimate along the bars. This averaged strain value formed the baseline pre-test loading on the specimen. Direct shear tests were conducted using a servo-hydraulic universal testing machine with close loop control of displacement. Two units of LVDTs were fixed to the concrete cover at the top edge of the SRG bond. The front facing LVDTs (termed herein as LVDT_FR and LVDT_FL for front-right and front-left positions, respectively) were supported by a thin U-shaped aluminium plate affixed to the composite adjoining the start of the bonding area. In this work, two types of displacement measurements were recorded. One was slip, which was defined as the average of the LVDT_FR and LVDT_FL responses (termed herein as LVDT_Fave). Slip acted as both displacement control and measurement variable. The other measurement was the upper grips displacement of the machine head (termed herein as UG). A slip rate of 0.00084 mm/s was administered as the standard rate for the majority of tests. Some tests were performed using different rates equivalent to half (0.00042 mm/s) and 10 times (0.0084 mm/s) the standard rate to investigate the influence of the test rate on the debonding mechanism.

In addition, two back facing LVDTs (termed herein as LVDT_BR and LVDT_BL in the same fashion as the front transducers) were positioned perpendicular to the composite surface to gauge the lateral displacement of the test specimen. Both LVDTs mounts were secured by strong magnets and positioned parallel to the surface of the composite. The point of this response taking was estimated to be at a distance of 300 mm from the concrete block's bottom surface. These measurements represent the magnitude of rotation potentially caused by loading eccentricity during the tests.

In testing the effects of varying fibre densities, the bonded length (Fig. 1(a)) and bond width (b_f) remained unchanged at 200 mm and 50 mm, respectively, for specimens strengthened with LD fibre strips and 450 mm and 50 mm, respectively, for specimens strengthened with MD and MHD fibre strips. For reporting purposes, the test specimens were labelled according to the notation of S_A_Rr_X. A indicates the fibre density (LD , MD and MHD, as described earlier). Rr represents the load rate, whereby R1 = 0.00084 mm/s is the standard rate used for this work. The letter 'r' in Rr varies according to the rate ratio with respect to the standard rate (R1). For instance, R0.5 denotes the value of 0.00042 mm/s (which is half of R1) whereas R10 denotes the value 0.0084 mm/s (which is 10 times of R1). Lastly, X demonstrates the specimen number. The direct shear test results including load capacity (P_{max}) average values and coefficient of variations (as percentage in parenthesis) are presented in Table 3. Pictures of representative test specimens with different density of steel sheets are shown in Fig. 2.

Table 3 Experimental direct shear test results

Series	Specimen name	P_{max} (kN)		σ_{max} (Mpa)	Slip (P_{max}) (mm)	UG (P_{max}) (mm)	BL(P_{max}) (mm)	BR(P_{max}) (mm)	Failure Mode	n
	S_LD_R1_1	13.15		3055	1.33	8.13	*	*	FR	8
LD_R1	S_LD_R1_2	13.23	13.23 (0.60%)	3074	1.51	7.72	0.2073	0.0004	FR	8
	S_LD_R1_3	13.31		3092	1.25	8.29	0.6046	0.4407	FR	8
	S_MD_R1_1	10.98		1701	0.64	3.79	0.6824	0.6199	MF	12
MD_R1	S_MD_R1_2	13.18	11.67 (11.25%)	2042	2.34	6.48	0.5244	0.5083	MF	12
	S_MD_R1_3	10.84		1679	0.63	3.77	0.3671	0.3338	MF	12
	S_MHD_R1_1	7.90		918	0.39	2.21	0.2177	0.1251	MF	16
MHD_R1	S_MHD_R1_2	7.58	8.10 (5.87%)	881	0.82	2.40	0.0001	0.0006	MF	16
	S_MHD_R1_3	8.69		1010	0.35	2.16	0.1382	0.1015	MF	16
	S_MHD_R1_4	8.24		957	0.34	2.11	0.0890	0.0664	MF	16
	S_MD_R10_1	12.21		1891	0.61	4.27	0.8073	0.7428	MF	12
MD_R10	S_MD_R10_2	11.73	12.25 (4.46%)	1817	0.59	4.27	0.5822	0.5605	MF	12
	S_MD_R10_3	12.82		1986	2.20	5.93	0.4424	0.4179	MF	12
	S_MHD_R10_1	7.90		918	0.59	2.06	0.0591	0.0295	MF	16
MHD_R10	S_MHD_R10_2	9.02	8.64 (7.39%)	1048	0.28	2.14	0.0956	0.0812	MF	16
	S_MHD_R10_3	8.99		1044	0.37	2.27	0.2211	0.1659	MF	16
MD_R0.5	S_MD_R0.5_1	11.42	11.19 (2.91%)	1769	2.72	6.30	0.1393	0.4499	MF	12
	S_MD_R0.5_2	10.96		1698	3.22	6.51	0.1341	0.1831	MF	12
	S_MHD_R0.5_1	6.75		784	1.61	3.17	0.0262	0.0501	MF	16
MHD_R0.5	S_MHD_R0.5_2	5.70	6.87 (17.97%)	662	0.42	1.59	0.0035	0.0005	MF	16
	S_MHD_R0.5_3	8.16		948	0.93	2.64	0.0571	0.0159	MF	16

* Back facing LVDTs (LVDT_BR and LVDT_BL) were not mounted on specimen

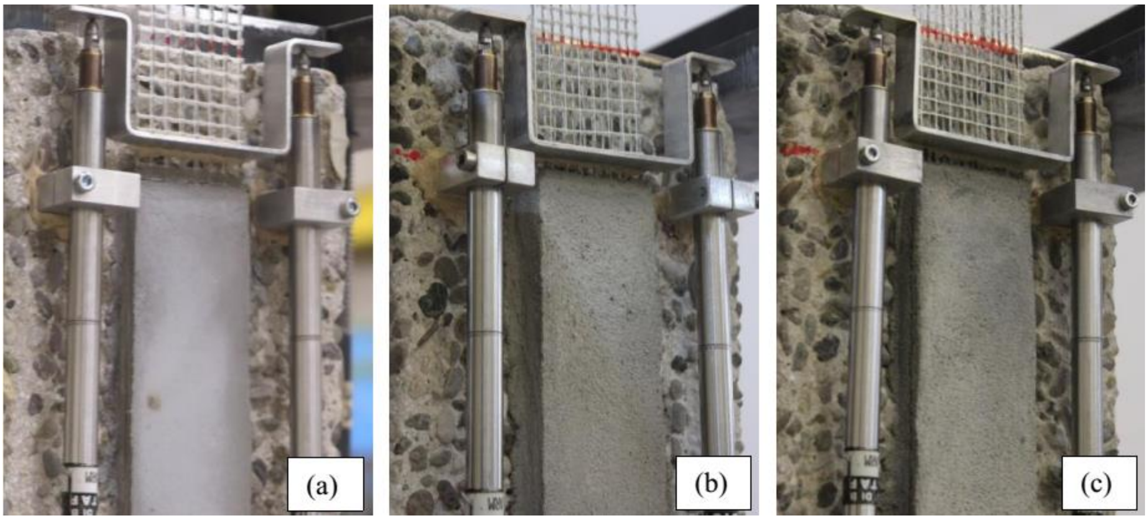

Fig. 2 Three different fiber densities in representative specimens: (a) Low density (S_LD_R1_3), (b) Medium density (S_MD_R1_2) and (c) Medium-high density (S_MHD_R1_2)

It is worthwhile to note that results from several testings were discarded due to the deformation and rotation of the aluminum U-shaped plate during the tests. These were attributed to uneven load distribution that occured among the fibers. Provision for specimens to be disregarded was made when the difference between the two front facing LVDTs was greater than 0.5 mm. The use of this limit was based on the matrix-fibre interfacial constitutive law.

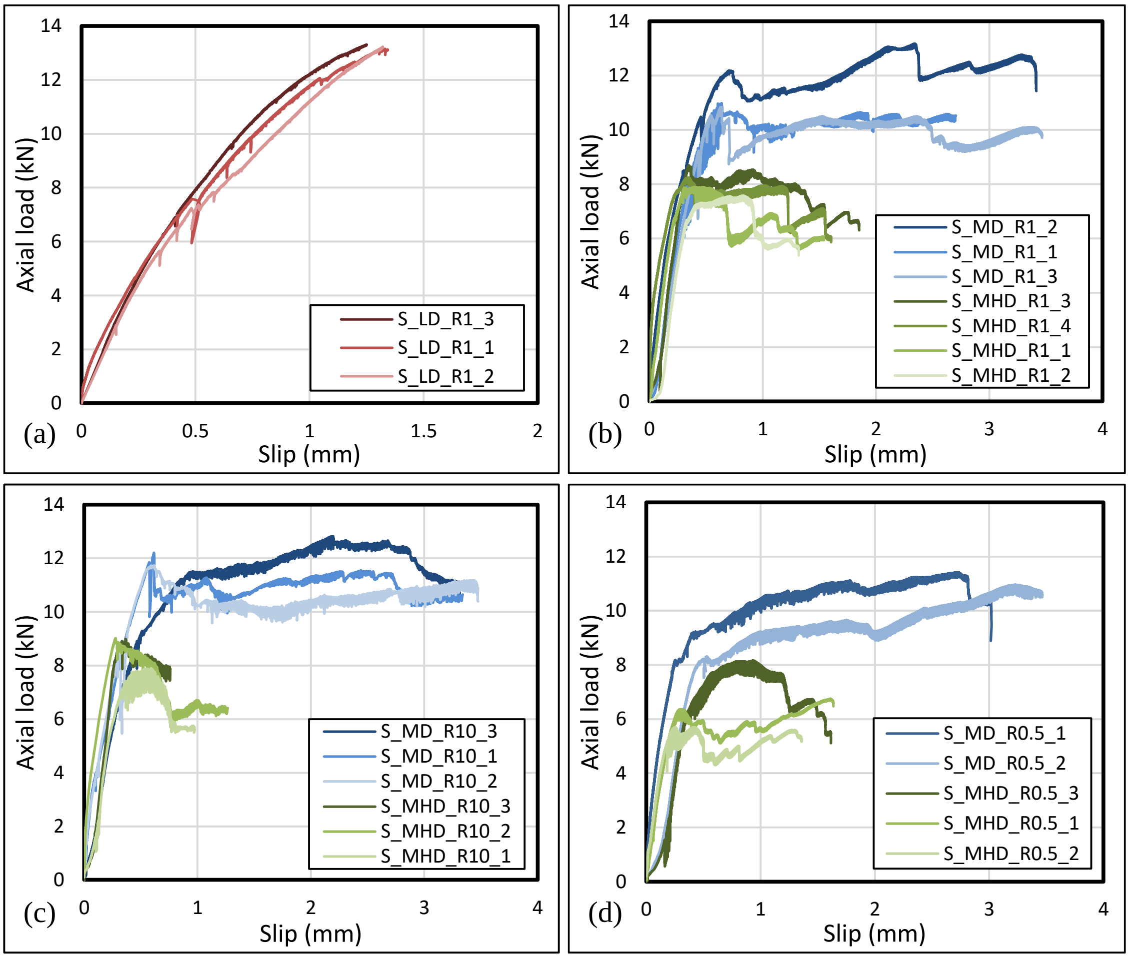

Fig. 3 Load response of specimen with the same rate ratios: (a) S_LD_R1 series, (b) S_MD_R1 and S_MHD_R1 series, (c) S_MD_R10 and S_MHD_R10 series and (d) S_MD_R0.5 and S_MHD_R0.5 series

3. Test results

3.1 Load responses

The load - slip responses of specimens strengthened with SRG composite corresponding to the same rate ratios and the same fibre densities are presented herein in Fig. 3 and Fig. 4, respectively.

A linear load response is first observed in Fig. 3(a) for the SRG specimens strengthened with LD fibres. The response subsequently progressed into a non-linear response up to the peak load (P_{max}), similarly, the load-slip response demonstrated consistent increments until the peak load (P_{max}) is achieved. With the SRG specimens strengthened with MD and MHD fibres (Figs. 3(b)-3(d)), the non-linear load responses plateaued, arriving at high values of slip before failure. The initial linear responses are representative of the elastic characteristics of the fibre-matrix bond, whereby the subsequent decline in stiffness is attributed to the micro-damages inflicted onto the interfacial fibre-matrix surfaces. Upon peak load (P_{max}), any additional increments in slip would induce a plateau state of applied load and consequently, lead to an abrupt decline of load with no post-peak softening responses. Both peak load (P_{max}) and its correlative ultimate stress (σ_{max}) for each specimen are detailed in Table 3. Ultimate stress (σ_{max}) denotes the stress at peak load (P_{max}) and is prescribed in Eq. (1)

$$\sigma = \frac{P}{nA_{cord}} \tag{1}$$

In Eq. (1), P represents the load administered by the testing machine, n represents the sum of fibre cords (as detailed in Table 3) and A_{cord} represents the area of each cord, which is set to be 0.538 mm^2 in this work.

With reference to Table 3, Fig. 3(b), Figs. 3(c) and 3(d), records of P_{max} and σ_{max} appeared higher in specimens with MD fibre compared to specimens with MHD fibre. Moreover, specimens with MD fibre noted higher values of slip before failure compared to specimens with MHD fibre. Similarly, in the comparison of P_{max} and σ_{max} records for different test rates in Table 3 and Fig. 4, it could be deduced that an increase in the load rate entailed an increase in the peak value observed in both MD and MHD fibre specimens. This phenomenon is attributed to creep in the cementitious matrix, which is fairly affected by the load rate.

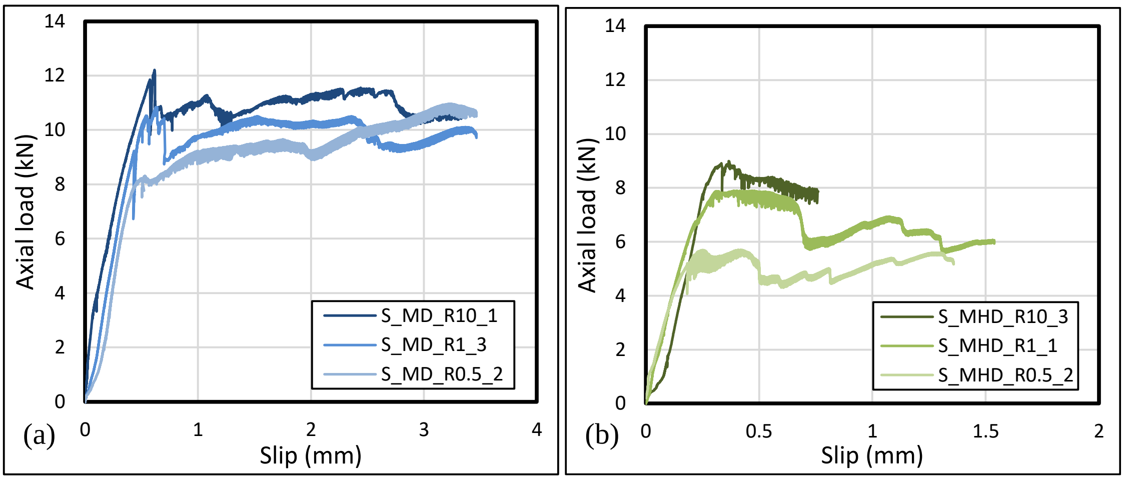

Fig. 4 Typical Load response of specimen with the same fibre density at different rate ratios: (a) typical specimens with MD fibre and (b) typical specimens with MHD fibre

Literature has revealed that FRP-concrete interfacial cracks form at the elastic, pre-peak area of responses. Unpredictable crack propagation consequent to peak load results in an acute decline in load (Park and Yoo 2013). Therefore, the recorded P_{max} could be a misrepresentation of load relating to steady crack growth in specimens with bonds larger than the prescribed effective length. The *P-slip* responses presented in Figs. 3 and 4 are notably comparable to other studies (Park and Yoo 2013, Li *et al.* 2014). The later state of unchanged in the load response observed implies that load-carrying capacity of the interface was fulfilled, and therefore, the bonded length ranged beyond the effective bond length (Kim and Aboutaha 2004, Nascimbene 2013, Ghiassi *et al.* 2016, Grande *et al.* 2018, Ascione *et al.* 2019). The definite value of effective bond length entails additional investigation, which is beyond the scope of this paper.

It should be noted that the load response of SRG composites is distinctively unique compare to other FRCM composite systems (Daskiran *et al.* 2016, Donnini and Corinaldesi 2017, Younis and Ebead 2018, Bellini *et al.* 2019). For instance, failure of SRG composites in this work is observed to have occurred at the fibre-matrix interface. Failure is linked to fracture of matrix at the fibre plane and slippage of fibre. Slip is comparatively miniscule at the initiation of debonding (approximately 10% that of a PBO-FRCM composite)(Trapko and Musiał 2017, Marcinczak *et al.* 2019). This is consistent with the separation of outer matrix layer and fibre strip with no softening response observed in Figs. 3 and 4. As for other FRCM composites, debonding is marked by substantial fibre slippage. Upon peak load, a bonded length beyond the effective bond length would lead to a softening response, and conclude with a non-zero load response. From a mechanical point of view, this phenomenon stemmed from fibre-matrix friction and interlocking fibre friction (Santandrea *et al.* 2016, Jahangir and Esfahani 2018). These observations revealed that further investigation on the stress transfer mechanism and influence of friction on load responses are necessary.

3.2 Mode of failures

In this work, two types of failure modes were observed for all specimens; namely fibre rupture (FR) and matrix – fibre detachment (MF). The corresponding failure mode for each specimen is detailed in Table 3. The former mode is generally pertinent to LD steel fibres. Failure of specimens with MD and MHD fibres are typified by debonding at the interfacial matrix-fibre substrate and matrix fracture between the fibres. The brittle separation of fibre layers and external matrix cover is often acute. Fig. 5 demonstrates typical specimens with typical FR and MF failure modes.

The sighting of transversal hairline cracks in the matrix of SRG composite specimens with MD and MHD fibres is attributed to the buildup in fibre slippage. As the specimens are loaded, fibre slippage at the internal matrix layer takes place. At the same time, the external matrix layer (which is bonded to the fibres) slips relative to the internal matrix layer (which is bonded to the concrete substrate). Cracks are usually initiated close to the loaded edge of the composite before growing steadily towards the composite-free side. The cracks are observed to have spread from the external layer of the composite to the fibre strip. This analysis on failure modes highlights the influence of fibre density in SRG specimens. The difference in the types of rupture could be attributed to the reduced area of mortar in between the fibre bundles, which inherently lowers the peak load of MHD fibre specimens in comparison to the MD ones.

4. Discussion

This work examines the influences of three loading rates and three different fibre densities, as described in Table 3. Two categories of measurement, slip and machine grips, were considered for each specimen.

Slip acted as a test control and was derived by methodically raising the mean readings of two front facing LVDTs (LVDT_FR and LVDT_FL). Machine grips, or

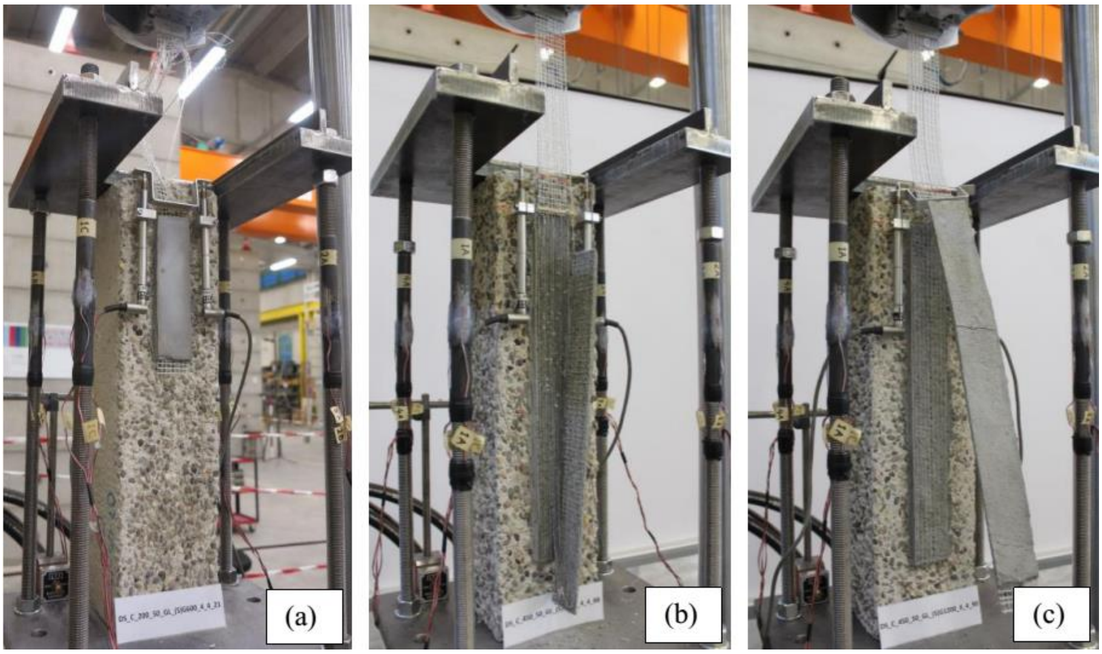

Fig. 5 Predominant modes of failure in direct shear tests (a): Rupture of fibres (S_LD_R1_3), (b): matrix-fiber interface debonding (S_MD_R1_1) and (c): matrix-fiber interface debonding (S_MHD_R1_1)

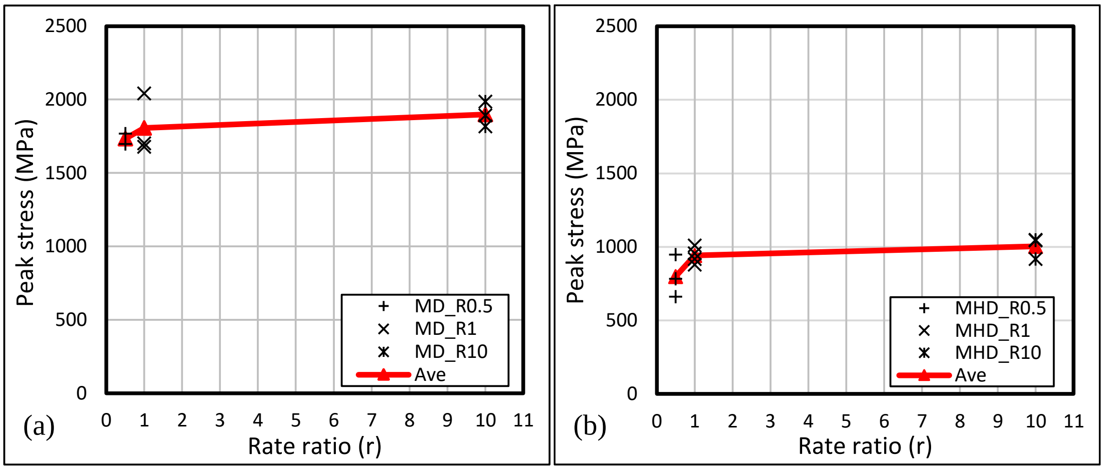

Fig. 6 Peak stress (σmax) versus rate ratio (r) for specimens with different fibre densities: (a) MD density series and (b) MHD density series

machine upper grips (UG), denoted the displacement readings obtained by an LVDT insert at the machine head. The following section discusses the effects of load rate as well as density of fibres with reference to peak stress (σ_{max}), slip and UG readings, and average of two back facing LVDTs (LVDT_BR and LVDT_BL) readings at peak load (P_{max}). The influence of measurement type is also examined.

4.1 Peak stress

Fig. 6 shows the peak stress (σ_{max}) versus rate ratio (r) for specimens with MD and MHD fibre. The trend line of the ratio is depicted in red, linking the average value of each rate ratio.

In correspondence to the rise in rate ratio from 0.5 to 10, peak stress (σ_{max}) rises in two separate ascending branches, one from rate ratio between R0.5 to R1 and the other between R1 to R10. The maximum average σ_{max} is observed at rate ratio R10. Comparatively, the gradient of the first branch is steeper and this observation is analogous for both fibre densities (MD and MHD). The peak stresses in MD fibre specimens are higher than MHD fibre specimens for each rate.

4.2 Slip at peak load

Fig. 7 shows the average front LVDTs displacement (slip) at peak load for specimens with MD and MHD fibre

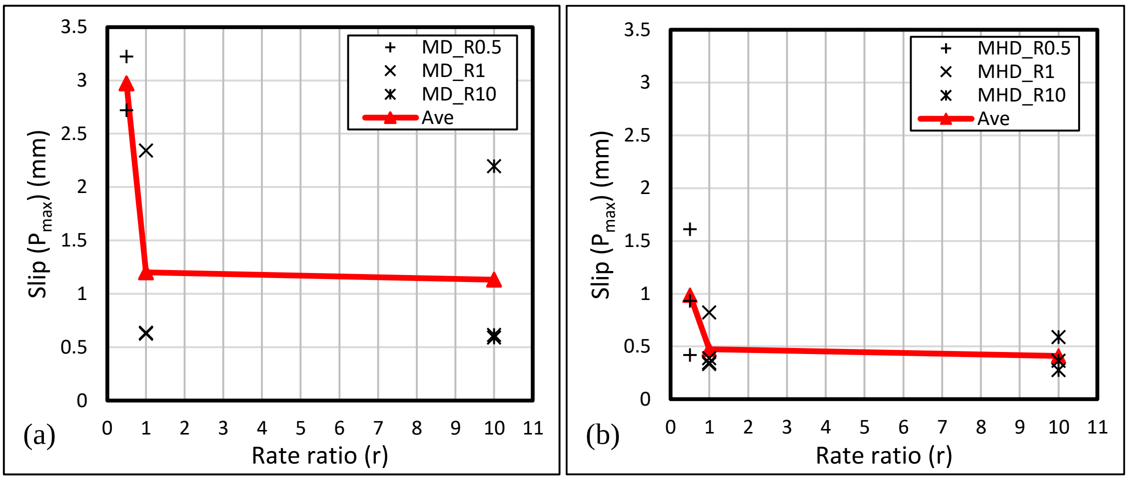

Fig. 7 Slip at peak load (Pmax) versus rate ratio (r) for specimens with different fibre densities: (a) MD density series and (b) MHD density series

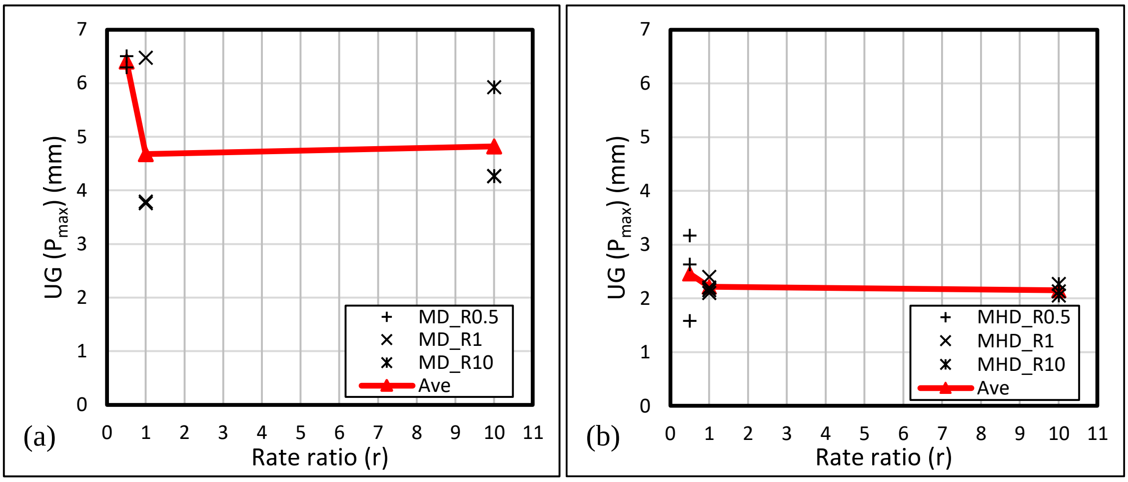

Fig. 8 Upper grip displacement (UG) reading at peak load (Pmax) versus rate ratio (r) for specimens with different fibre densities: (a) MD density series and (b) MHD density series

versus rate ratio (r). The trend line of the ratio is depicted in red, linking the average value of each rate ratio.

For both MD and MHD fibre specimens, the plotted trend reveals a decline in slip corresponding to peak load vs the rate ratio. Similar to peak stress, the gradient of the first descending branch (for rate ratio R0.5 to R1) is steeper and this observation is analogous for both fibre densities (MD and MHD fibre). Due to the failure modes, the slip at peak load in MD fibre specimens is higher than MHD fibre specimens for rates R0.5 to R10.

4.3 Upper grips displacement at peak load

Fig. 8 shows the upper grip displacement readings (UG) corresponding to peak load for specimens with MD and MHD fibre versus rate ratio (r). Similar to previous sections (Section 4.1 and 4.2), the trend line of the ratio is depicted in red, linking the average value of each rate ratio.

For the MD fibre density specimens, the UG at peak load versus rate ratio is represented by a descending branch (from rate ratio R0.5 to R1) of higher gradient and an ascending branch (from rate ratio R1 to R10) of a lower gradient. Comparatively, for the MHD fibre density specimens, the average trend of UG at peak load versus rate ratio is characterized by two descending branches (from R0.5 to R1 and R1 to R10). There is no clear observable trend for the UP versus r relationship, in agreement to Salimian and Mostofinejad (2019). It was inferred that there is no distinct relationship definition between slip corresponding to maximum shear stress and strain rate.

4.4 Back LVDTs displacement at peak load

As mentioned in Section 2.2, back facing LVDTs (LVDT_BR and LVDT_BL) secured perpendicular to the surface of the strip were used to measure the extent of rotation and probable loading eccentricity during the

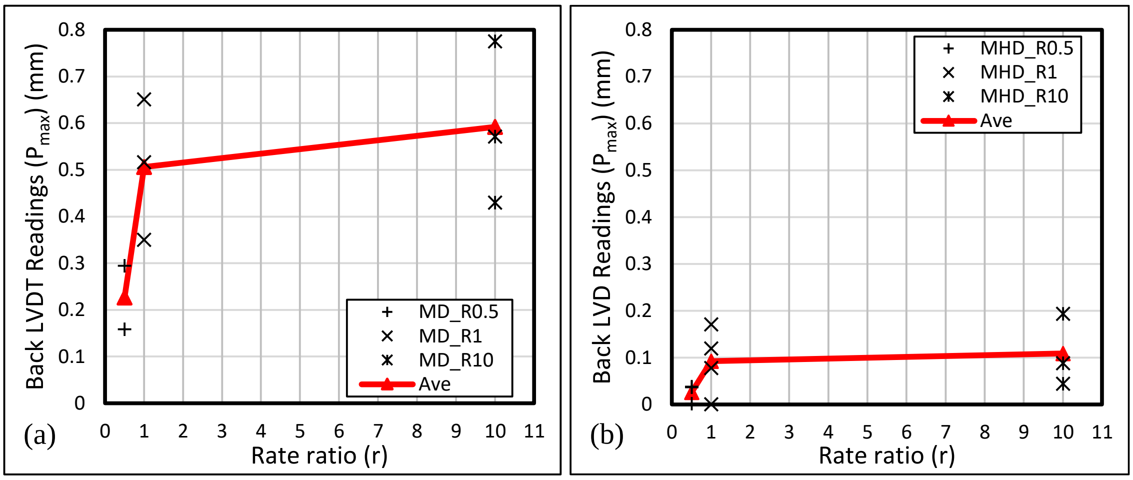

Fig. 9 Average back LVDTs displacement readings at peak load (Pmax) versus rate ratio (r) for specimens with different fibre densities: (a) MD density series and (b) MHD density series

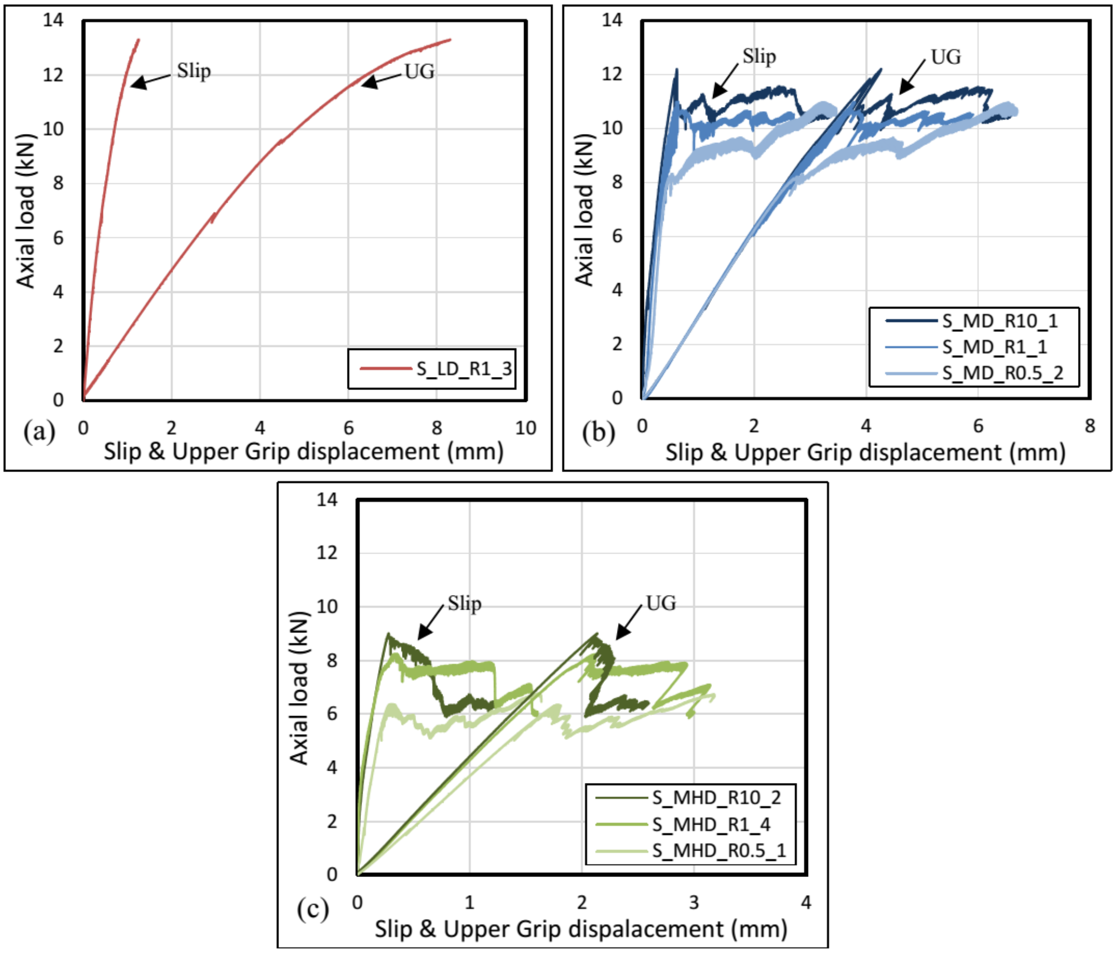

Fig. 10 Typical load versus average front LVDTs (Slip) or upper grips displacement (UG) response for specimens tested at different rates and with different fibre densities: (a) LD density; (b) MD density; and (c) MHD density

experiments. The displacements BL(P_{max}) and BR(P_{max}) associated to the peak load P_{max}, as measured by LVDT_BL, and LVDT_BR, respectively, are presented in Table 3. Fig. 9 presents the average readings of BL(P_{max}) and BR(P_{max}) (termed Ave_B), with respect to loading rate ratios, for each group of specimens with MD and MHD fibre.

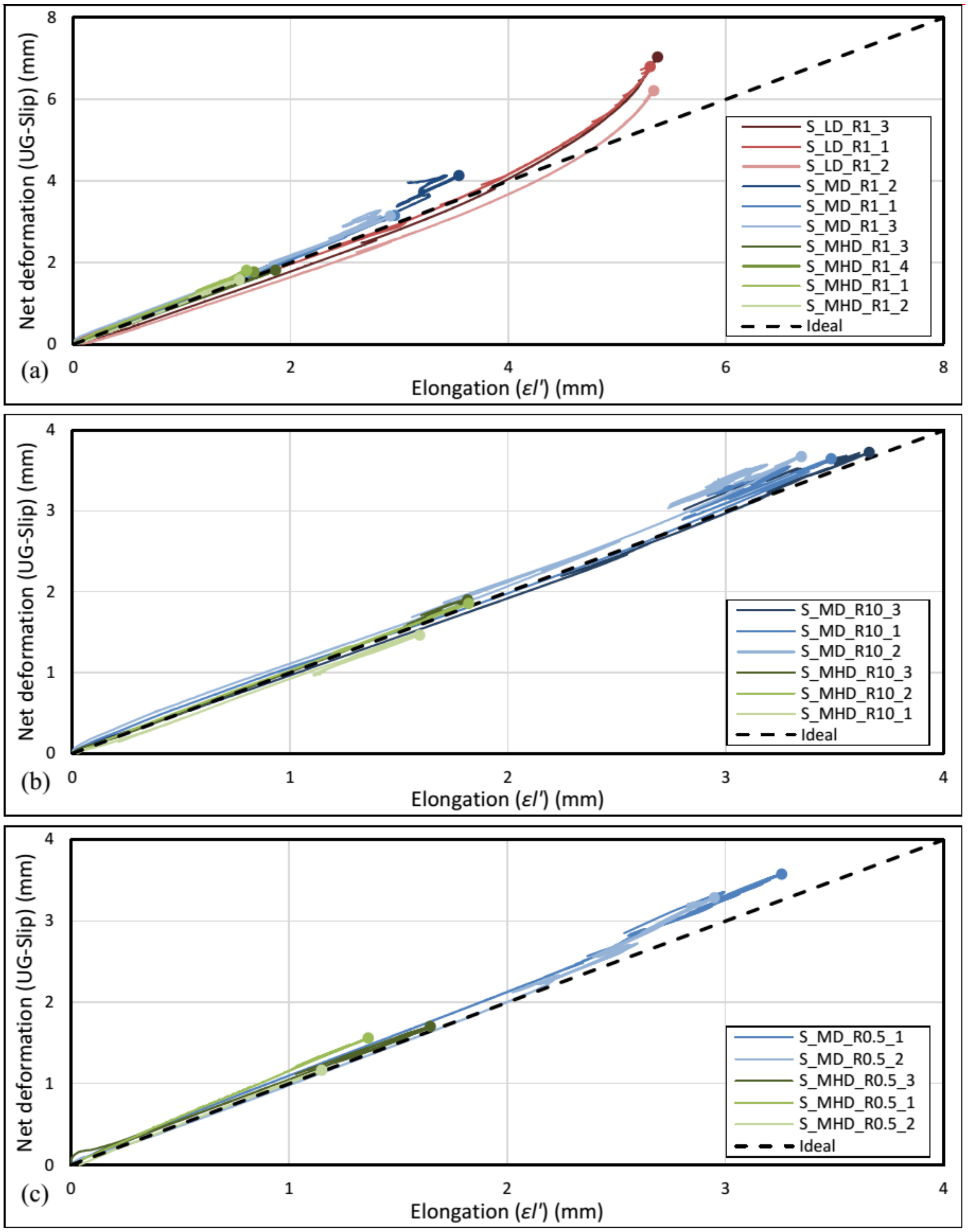

Fig. 11 Comparison of Net deformation (UG-Slip) versus elongation ($\varepsilon l'$) determined from Eq. (2) for specimens with different fibre density at different rates: (a) R1 series, (b) R10 series and (c) R0.5 series

For both MD and MHD fibre, it is observed that the Ave_B displacements at peak load rises with the intensification of rate ratio. As all out-of-plane displacements at peak load were noted to be below 1 mm, the Mode-I parameter could have been overlooked in the recordings of BL(P_{max}) and BR(P_{max}) in Table 3.

4.5 Effect of measurement type

Fig. 10 presents the load responses of representative specimens with different fibre densities tested at varying rates. The responses are charted with reference to axial load versus the average readings of the two front LVDTs (Slip) and axial load versus the displacement measured by upper grips (UG) at machine head.

It is evident in Fig. 10 that the initial stiffness readings of load versus upper grips (UG) are relatively lower to those of load versus average front facing LVDTs (Slip). Readings for the former test vary throughout the measurements due to the deformation of exposed fibres beyond the bonded area. The longitudinal strain ε in bare fibers for any load P can be calculated using Eq. (2)

$$\varepsilon = \frac{P}{nA_{cord}E_f} \tag{2}$$

By which E_f denotes the elastic modulus of fibers (as reported in Table 1 and was considered equal to 200 GPa in Eq. (2)). l' is defined as the distance between the grips and onset of the composite at the bonded area where the U-shaped plate was administered. In this work, it measures 330 mm. The difference between the upper grip displacement reading (UG) and the average front LDVTs measured and controlled displacement (Slip) can be approximated using Eq. (3)

$$UG - Slip = \varepsilon l' \tag{6}$$

As the transducers are secured to the machine head, a new term should be included in Eq. (3) to enumerate deformation of the machine heads.

Fig. 11 showcases the difference in UG-Slip of the load responses of every specimens versus $\varepsilon l'$. ε can be computed using Eq. (2). Readings corresponding to peak load P_{max} are featured as points for every specimen, with the exception to specimens of low fibre density (S_LD_R1 series). This is due to the non-linear behaviour exhibited by the bare fibres prior to rupture. On the contrary, a fair level of agreement between the left and right sides of Eq. (3) up till peak load is noted for other specimens of different densities. Nevertheless, the occurrence of local debonding could affect the efficiency of Eq. (3).

5. Conclusions

The outcomes of an investigation into the interfacial characteristics of steel reinforced grout (SRG) composite strips adhered to concrete prisms was reported. Direct-shear tests were conducted at three different loading rates. Three varying densities of SRG composite strips and two categories of measurement, slip and machine grips, respectively, were examined. The ensuing commentary concludes this investigative work:

- Rupture of the fibres was noted in the SRG-concrete joints samples with low density steel fibres. The modes of failures observed for samples of medium density (MD) and medium-high density (MHD), include fibre slippage and fracture of matrix at the interfacial region of the internal matrix and fibre. In contrast to alternative FRCM systems, post-peak softening responses were not recorded.
- It was observed that peak load P_{max} and corresponding peak stress σ_{max} increased as the slip rate was raised. This trend was analogous for both MD and MHD steel fibres. As expected, the measured value of peak stresses are greater in lower density of fibre series with respect to higher density of fibre series for all loading rates.
- Slip correlative to the peak load decreased as the loading rate increased for both MD and MHD fibre series. For all loading rates, the slip at peak load observed in MD fibre series were higher than MHD fibre series. This was attributed to the nature of their failure modes.
- There was no distinct trend for UG displacement responses correlative to peak load, with reference to changes in loading rate.
- The average value of the out-of-plane displacements at peak load increased with increments in load rates, independent of specimen fibre densities. Despite the increase, values remained small. Therefore, the Mode-I component for all specimens (with composite bond length of 200 mm and 450 mm) could be overlooked.
- Initial stiffness is affected by the type of measurement variables. In consequence of the deformation of bare fibres beyond the bonded region, initial stiffness of load versus UG measurements were lower compared to those of initial stiffness of load versus slip measurements.

Acknowledgments

The authors convey sincere appreciations to Dr. Christian Carloni, as well as the technicians of LISG (Laboratory of Structural and Geotechnical Engineering) and CIRI (Interdepartmental Centre for Industrial Research in Building and Construction) for sharing their knowledge and wisdom throughout this research during the first author's sabbatical leave at University of Bologna, Italy. Also not forgetting Kerakoll of Sassuolo, Italy, whom the authors acknowledge for providing composite materials for testing.

References

Abderezak, R., Daouadji, T.H., Rabia, B. and Belkacem, A. (2018), "Nonlinear analysis of damaged RC beams strengthened with glass fiber reinforced polymer plate under symmetric loads", *Earthq. Struct.*, **15**(2), 113–122. https://doi.org/10.12989/eas.2018.15.2.113.

ACI 440.2R (2008), Guide for the Design and Construction of Externally Bonded FRP Systems; American Concrete Institute.

Aggelis, D.G., Verbruggen, S., Tsangouri, E., Tysmans, T., and Van Hemelrijck, D. (2016), "Monitoring the failure mechanisms of a reinforced concrete beam strengthened by textile reinforced cement using acoustic emission and digital image correlation", *Smart Struct. Syst.*, **17**(1), 91–105. https://doi.org/10.12989/sss.2016.17.1.091.

Alecci, V., Misseri, G., Rovero, L., Stipo, G., De Stefano, M., Feo, L. and Luciano, R. (2016), "Experimental investigation on masonry arches strengthened with PBO-FRCM composite", *Compos. Part B: Eng.*, **100**, 228-239. https://doi.org/10.1016/j.compositesb.2016.05.063.

Amidi, S. and Wang, J. (2016), "Subcritical debonding of FRP-to-concrete bonded interface under synergistic effect of load, moisture, and temperature", *Mech. Mater.*, **92**, 80-93. https://doi.org/10.1016/j.mechmat.2015.09.001.

Ascione, F., Lamberti, M., Napoli, A., Razaqpur, A.G. and Realfonzo, R. (2019), "Modeling SRP-concrete interfacial bond behavior and strength", *Eng. Struct.*, **187**, 220-230. https://doi.org/10.1016/j.engstruct.2019.02.050.

Ascione, F., Lamberti, M., Napoli, A., Razaqpur, G. and Realfonzo, R. (2017), "An experimental investigation on the bond behavior of steel reinforced polymers on concrete substrate", *Compos. Struct.*, **181**, 58-72. https://doi.org/10.1016/j.compstruct.2017.08.063.

Babatunde, S.A. (2017), "Review of strengthening techniques for masonry using fiber reinforced polymers", *Compos. Struct.*, **161**, 246-255. https://doi.org/10.1016/j.compstruct.2016.10.132.

Bagheri, M., Chahkandi, A. and Jahangir, H. (2019), "Seismic Reliability Analysis of RC Frames Rehabilitated by Glass Fiber-Reinforced Polymers", *Int. J. Civil Eng.*, **17**(11), 1785-1797. https://doi.org/10.1007/s40999-019-00438-x.

Barakat, S., Al-Toubat, S., Leblouba, M. and Al Burai, E. (2019), "Behavioral trends of shear strengthened reinforced concrete beams with externally bonded fiber-reinforced polymer", *Struct. Eng. Mech.*, **69**(5), 579-589. https://doi.org/10.12989/sem.2019.69.5.579.

Bellini, A., Bovo, M. and Mazzotti, C. (2019), "Experimental and numerical evaluation of fiber-matrix interface behaviour of different FRCM systems", *Compos. Part B: Eng.*, **161**, 411–426. https://doi.org/10.1016/j.compositesb.2018.12.115.

Bencardino, F. and Condello, A. (2014), "Experimental study and numerical investigation of behavior of RC beams strengthened with steel reinforced grout", *Comput. Concrete*, **14**(6), 711-725. https://doi.org/10.12989/cac.2014.14.6.711.

Borri, A., Casadei, P., Castori, G. and Hammond, J. (2009), "Strengthening of Brick Masonry Arches with Externally Bonded Steel Reinforced Composites", *J. Compos. Constr.*, **13**(6), 468-475. https://doi.org/10.1061/(ASCE)CC.1943-5614.0000030.

Cao, M., Li, L. and Xu, L. (2017), "Relations between rheological and mechanical properties of fiber reinforced mortar", *Comput. Concrete*, **20**(4), 449-459. https://doi.org/10.12989/cac.2017.20.4.449.

Carozzi, F.G., Poggi, C., Bertolesi, E. and Milani, G. (2018), "Ancient masonry arches and vaults strengthened with TRM, SRG and FRP composites: Experimental evaluation", *Compos. Struct.*, **187**, 466-480. https://doi.org/10.1016/j.compstruct.2017.12.075.

Casadei, P. and Girardello, P. (2019), "SRG Composite Systems for Strengthening Masonry Structures: From Laboratory to Field Applications." In *Structural Analysis of Historical Constructions*, 1715-1724. Springer, Cham.

Daskiran, E.G., Daskiran, M.M. and Gencoglu, M. (2016), "Development of fine grained concretes for textile reinforced cementitious composites", *Comput. Concrete*, **18**(2), 279-295. https://doi.org/10.12989/cac.2016.18.2.279.

De Canio, G., de Felice, G., De Santis, S., Giocoli, A., Mongelli, M., Paolacci, F. and Roselli, I. (2016), "Passive 3D motion optical data in shaking table tests of a SRG-reinforced masonry wall", *Earthq. Struct.*, **10**(1), 53-71. https://doi.org/10.12989/eas.2016.10.1.053.

De Santis, S., Ceroni, F., de Felice, G., Fagone, M., Ghiassi, B., Kwiecień, A., Lignola, G.P., Morganti, M., Santandrea, M., Valluzzi, M.R. and Viskovic, A. (2017), "Round Robin Test on tensile and bond behaviour of Steel Reinforced Grout systems", *Compos. Part B: Eng.*, **127**, 100-120. https://doi.org/10.1016/j.compositesb.2017.03.052.

De Santis, S., de Felice, G., Napoli, A. and Realfonzo, R. (2016), "Strengthening of structures with Steel Reinforced Polymers: A state-of-the-art review", *Compos. Part B: Eng.*, **104**, 87-110. https://doi.org/10.1016/j.compositesb.2016.08.025.

De Santis, S., Hadad, H.A., De Caso y Basalo, F., de Felice, G., and Nanni, A. (2018), "Acceptance criteria for tensile characterization of fabric-reinforced cementitious matrix systems for concrete and masonry repair", *J. Compos.r Constr.*, **22**(6), 04018048. https://doi.org/10.1061/(ASCE)CC.1943-5614.0000886.

De Santis, S., Roscini, F. and de Felice, G. (2019). "Strengthening of masonry vaults with textile reinforced mortars." In *Structural Analysis of Historical Constructions*, 1539-1547, Springer, Cham.

Donnini, J. and Corinaldesi, V. (2017), "Mechanical characterization of different FRCM systems for structural reinforcement", *Constr. Building Mater.*, **145**, 565-575. https://doi.org/10.1016/j.conbuildmat.2017.04.051.

EN, B.S. (2009), Testing hardened concrete--Part 3: Compressive strength of test specimens; London, British Standard Institution.

Ghiassi, B., Oliveira, D.V., Marques, V., Soares, E. and Maljaee, H. (2016), "Multi-level characterization of steel reinforced mortars for strengthening of masonry structures", *Mater. Design*, **110**, 903-913. https://doi.org/10.1016/j.matdes.2016.08.034.

Grande, E., Imbimbo, M. and Sacco, E. (2015), "Investigation on the bond behavior of clay bricks reinforced with SRP and SRG strengthening systems", *Mater. Struct.*, **48**(11), 3755-3770. https://doi.org/10.1617/s11527-014-0437-x.

Grande, E., Imbimbo, M. and Sacco, E. (2018), "Numerical investigation on the bond behavior of FRCM strengthening systems", *Compos. Part B: Eng.*, **145**, 240-251. https://doi.org/10.1016/j.compositesb.2018.03.010.

Hadji, L., Daouadji, T.H., Meziane, M.A.A. and Bedia, E.A.A. (2016), "Analyze of the interfacial stress in reinforced concrete beams strengthened with externally bonded CFRP plate", *Steel Compos. Struct.*, **20**(2), 413-429. https://doi.org/10.12989/scs.2016.20.2.413.

Huang, J. and Huang, P. (2011), "Three-dimensional numerical simulation and cracking analysis of fiber-reinforced cement-based composites", *Comput. Concrete*, **8**(3), 327-341. https://doi.org/10.12989/cac.2011.8.3.327.

Huang, X., Birman, V., Nanni, A. and Tunis, G. (2005), "Properties and potential for application of steel reinforced polymer and steel reinforced grout composites", *Compos. Part B: Eng.*, **36**(1), 73-82. https://doi.org/10.1016/S1359-8368(03)00080-5.

Jabbar, A.S.A., Alam, M.A. and Mustapha, K.N. (2016), "Investigation of the effects of connectors to enhance bond strength of externally bonded steel plates and CFRP laminates with concrete", *Steel Compos. Struct.*, **20**(6), 1275-1303. https://doi.org/10.12989/scs.2016.20.6.1275.

Jabr, A., El-Ragaby, A. and Ghrib, F. (2017), "Effect of the fiber type and axial stiffness of FRCM on the flexural strengthening of RC beams", *Fibers*, **5**(1), 2-16. https://doi.org/10.3390/fib5010002.

Jahangir, H. and Esfahani, M.R. (2018), "Numerical study of bond – slip mechanism in advanced externally bonded strengthening composites", *KSCE J. Civil Engineering*, **22**(11), 4509-4518. https://doi.org/10.1007/s12205-018-1662-6.

Jiang, S., Guo, X., Xiong, Z., Cai, Y. and Zhu, S. (2017), "Experimental studies on behaviour of tubular T-joints reinforced with grouted sleeve", *Steel Compos. Struct.*, **23**(5), 585-596. https://doi.org/10.12989/scs.2017.23.5.585.

Kerakoll, S.P.A. (2018), http://www.kerakoll.com

Kim, S.H., and Aboutaha, R.S. (2004), "Ductility of carbon fiber-reinforced polymer (CFRP) strengthened reinforced concrete beams: Experimental investigation", *Steel Compos. Struct.*, **4**(5),

333-353. https://doi.org/10.12989/scs.2004.4.5.333.
Koksal, H.O., Jafarov, O., Doran, B., Aktan, S. and Karakoc, C. (2013), "Computational material modeling of masonry walls strengthened with fiber reinforced polymers", *Struct. Eng. Mech.*, **48**(5), 737-755. https://doi.org/10.12989/sem.2013.48.5.737.
Koutas, L.N., Tetta, Z., Bournas, D.A. and Triantafillou, T.C. (2019), "Strengthening of concrete structures with textile reinforced mortars: State-of-the-art review", *J. Compos. Constr.*, **23**(1), 03118001. https://doi.org/10.1061/(ASCE)CC.1943-5614.0000882.
Kwon, S.J., Choi, J.I., Nguyen, H.H. and Lee, B.Y. (2018), "Tensile strain-hardening behaviors and crack patterns of slag-based fiber-reinforced composites", *Comput. Concrete*, **21**(3), 231-237. https://doi.org/10.12989/cac.2018.21.3.231.
Li, H., Wang, W. and Zhou, W. (2014), "Fatigue damage monitoring and evolution for basalt fiber reinforced polymer materials", *Smart Struct. Syst.*, **14**(3), 307-325. https://doi.org/10.12989/sss.2014.14.3.307.
Li, S.C., Dong, J.X. and Li, L.F. (2012), "Experimental hysteretic behavior of in-plane loaded reinforced grouted multi-ribbed aerated concrete blocks masonry walls", *Struct. Eng. Mech.*, **41**(1), 95-112. https://doi.org/10.12989/sem.2012.41.1.095.
Liang, X. and Xing, P. (2018), "Seismic behavior of fiber reinforced cementitious composites coupling beams with conventional reinforcement", *Earthq. Struct.*, **14**(3), 261-271. https://doi.org/10.12989/eas.2018.14.3.261.
Lopez, A., Galati, N., Alkhrdaji, T. and Nanni, A. (2007), "Strengthening of a reinforced concrete bridge with externally bonded steel reinforced polymer (SRP)", *Compos. Part B: Eng.*, **38**(4), 429-436. https://doi.org/10.1016/j.compositesb.2006.09.003.
Marcinczak, D., Trapko, T. and Musiał, M. (2019), "Shear strengthening of reinforced concrete beams with PBO-FRCM composites with anchorage", *Compos. Part B: Eng.*, **158**, 149-161. https://doi.org/10.1016/j.compositesb.2018.09.061.
Mazzuca, S., Hadad, H.A., Ombres, L. and Nanni, A. (2019), "Mechanical characterization of steel-reinforced grout for strengthening of existing masonry and concrete structures", *J. Mater. Civil Eng.*, **31**(5), 04019037. https://doi.org/10.1061/(ASCE)MT.1943-5533.0002669.
Nascimbene, R. (2013), "Analysis and optimal design of fiber-reinforced composite structures: sail against the wind", *Wind Struct.*, **16**(6), 541-560. https://doi.org/10.12989/was.2013.16.6.541.
Park, J.G., Lee, K.M., Shin, H.M. and Park, Y.J. (2007), "Nonlinear analysis of RC beams strengthened by externally bonded plates", *Comput. Concrete*, **4**(2), 119-134. https://doi.org/10.12989/cac.2007.4.2.119.
Park, J.W. and Yoo, J.H. (2013), "Axial loading tests and load capacity prediction of slender SHS stub columns strengthened with carbon fiber reinforced polymers", *Steel Compos. Struct.*, **15**(2), 131-150. https://doi.org/10.12989/scs.2013.15.2.131.
Park, J., and Yoo, J. (2015), "Flexural and compression behavior for steel structures strengthened with Carbon Fiber Reinforced Polymers (CFRPs) sheet", *Steel and Composite Structures*, **19**(2), 441–465. https://doi.org/10.12989/scs.2015.19.2.441.
Pellegrino, C. and Modena, C. (2002), "Fiber reinforced polymer shear strengthening of reinforced concrete beams with transverse steel reinforcement", *J. Compos. Constr.*, **6**(2), 104-111. https://doi.org/10.1061/(ASCE)1090-0268(2002)6:2(104).
Prashob, P.S., Shashikala, A.P. and Somasundaran, T.P. (2017), "Behaviour of carbon fiber reinforced polymer strengthened tubular joints", *Steel Compos. Struct.*, **24**(4), 383-390. https://doi.org/10.12989/scs.2017.24.4.383.
Razavizadeh, A., Ghiassi, B. and Oliveira, D. V. (2014), "Bond behavior of SRG-strengthened masonry units: Testing and numerical modeling", *Constr. Build. Mater.*, **64**, 387-397. https://doi.org/10.1016/j.conbuildmat.2014.04.070.
Salimian, M.S. and Mostofinejad, D. (2019), "Experimental Evaluation of CFRP-Concrete Bond Behavior under High Loading Rates Using Particle Image Velocimetry Method", *J. Compos. Constr.*, **23**(3), 04019010. https://doi.org/10.1061/(ASCE)CC.1943-5614.0000933.
Santandrea, M., Imohamed, I.A.O., Jahangir, H., Carloni, C., Mazzotti, C., De Miranda, S., Ubertini, F. and Casadei, P. (2016). "An investigation of the debonding mechanism in steel FRP- and FRCM-concrete joints", *Proceedings of the 4th Workshop on The New Boundaries of Structural Concrete*, Capri, Italy, January.
Sumathi, A. and Vignesh, A.S. (2017), "Study on behavior of RCC beams with externally bonded FRP members in flexure", *Adv. Concrete Constr.*, **5**(6), 625-638. https://doi.org/10.12989/acc.2017.5.6.625.
Trapko, T. and Musiał, M. (2017), "PBO mesh mobilization via different ways of anchoring PBO-FRCM reinforcements", *Compos. Part B: Eng.*, **118**, 67-74. https://doi.org/10.1016/j.compositesb.2017.03.009.
Wang, X., Lam, C.C. and Iu, V.P. (2018), "Experimental investigation of in-plane shear behaviour of grey clay brick masonry panels strengthened with SRG", *Eng. Struct.*, **162**, 84-96. https://doi.org/10.1016/j.engstruct.2018.02.027.
Younis, A. and Ebead, U. (2018), "Bond characteristics of different FRCM systems", *Constr. Build. Mater.*, **175**, 610-620. https://doi.org/10.1016/j.conbuildmat.2018.04.216.

CC